ISTITUTO NAZIONALE DI RICERCA METROLOGICA
Repository Istituzionale

Nonharmonic Driving Fields for Enhancement of Nanoparticle Heating Efficiency in Magnetic Hyperthermia

(Article begins on next page)

28 April 2024

NON-HARMONIC DRIVING FIELDS FOR ENHANCEMENT OF NANOPARTICLE HEATING EFFICIENCY IN MAGNETIC HYPERTHERMIA

Paolo Allia[1,2],[*] Gabriele Barrera[1], and Paola Tiberto[1]

[1]*INRIM, Advanced Materials Metrology and Life Sciences,*

Strada delle Cacce 91, 10135 Torino, Italy and

[2]*DISAT, Politecnico di Torino, Corso Duca degli Abruzzi 24, I-10129 Torino, Italy*

[*] Corresponding author: paolo.allia@formerfaculty.polito.it

ABSTRACT

Applying non-harmonic driving field waveforms to nanoparticles for magnetic hyperthermia has beneficial effects on their ability to generate heating power. The response of superparamagnetic nanoparticles described as double-well systems with randomly distributed easy axes is studied by means of a rate-equation approach in the typical range of frequencies adopted in therapeutic applications. Magnetic hysteresis loops obtained at various frequencies and vertex fields show that sawtooth and square field waveforms substantially enhance the Specific Loss Power (SLP) with respect to a harmonic excitation of same frequency and amplitude. This improvement is related to the presence of fast, quasi-adiabatic transformations where the occupancy numbers in the two potential wells are virtually frozen, resulting in largely off-equilibrium magnetization states and in hysteresis loops with a greater area. The square driving field waveform is particularly promising for magnetic hyperthermia, the SLP being not only most effectively enhanced but also independent of particle size over a large interval of diameters. The special features of the hysteresis loops generated by the square driving field waveform are studied in detail; a peculiar effect of loop instability is described, and a condition for having stable hysteresis loops is defined. The considered driving field waveforms can be made to comply with the physiological restrictions imposed by magnetic hypertermia treatments *in vivo*.

I. INTRODUCTION

Magnetic hyperthermia for therapeutic use[1–7] is one of the most promising areas of application of magnetic nanoparticles[8–17]. The task of optimizing the performance of magnetic nanoparticles introduced in a living body poses a number of problems attaining physics, chemistry, biology, medicine[6,18–20] so that practical applications *in vivo* are still relatively limited in number and objectives[21]. On the other hand, growing interest is devoted to understanding how heat release from magnetic nanoparticles can be enhanced[22–27] .

In principle, magnetic hyperthermia of malignant tissues can be achieved exploiting both Brown's and Néel's relaxation processes[28]; however, in most cases (e.g., sufficiently small nanoparticles in a fluid, or immobilized particles) it is Néel's relaxation connected to intra-particle magnetization switching which dominates[29]. Therefore, adequately describing the dynamics of magnetization in nanoparticles submitted to an alternating field is a particularly important issue.

The most fundamental way to study the evolution of magnetic structures implies numerically solving the Landau-Lifshitz (LL)[30] or the Landau-Lifshitz-Gilbert (LLG)[31] equations. The approximations and shortcuts one needs to introduce can imply the cost of partly losing the grasp on the underlying physics, which can be an obstacle in practical applications.

In a simple yet effective approach the effect of thermal fluctuations on the magnetic state of a nanoparticle can be described in the context of the Néel model for thermally assisted (Arrhenius) magnetization reversal[32]. Uniaxial nanoparticles can be viewed as double-well systems[33,34] (DWS) where the particle's magnetic moment switches between the energy minima. In this context, rate equations are a most natural way to picture the effects stemming from the redistribution of moments in the energy wells by effect of temperature and/or magnetic field. These equations can be rigorously derived[35] from the Fokker−Planck equation proposed by Brown[36,37] for magnetization dynamics under the condition that the DWS barrier be high enough at all temperatures of interest (anisotropy energy > thermal energy), as is often the case. Rate equations have the advantage of giving a sufficiently accurate picture of the system's evolution without requiring much computational power and time. This approach has been successfully applied to study the response of magnetic nanoparticle submitted either to static[33] or time-dependent[30,38] magnetic fields.

In this paper, rate equations are exploited to study the effect of applying unconventional

driving-field waveforms on shape and area of the magnetic hysteresis loops generated by an assembly of nanoparticles with randomly directed easy-axis directions. In fact, in the large majority of papers on magnetic hyperthermia the driving field is assumed to be harmonic (AC excitation field)[4]. Only a few exceptions to this prevailing pattern exist[39,40]; however, these works, based on micromagnetic simulations, are mainly concerned with nanoparticle anisotropy and are not particularly useful to get insight in how the applied waveform can be modified in order to optimize the energy released by the nanoparticle to the environment.

Using rate equations naturally puts an upper limit to the range of driving-field frequencies. The highest escape frequency in the Arrhenius formalism is of the order of $10^9 - 10^{10}$ Hz[41], so the DWS assembly becomes increasingly non-responding as f approaches this limit; as a consequence, the highest frequency studied in this work is $f = 5 \times 10^5$ Hz, which is fully compatible with the state of the art of magnetic hyperthermia applications[4,21,29].

Although the role of interaction among nanoparticles is clearly not to be disregarded in magnetic hyperthermia[42–48], the present work is limited to the study of noninteracting particles, the emphasis being on the practical consequences of choosing a specific driving-field waveform on the actual performance of standard nanoparticles eligible for magnetic hyperthermia. It will be shown that even when nanoparticles do not interact a proper choice of the driving-field waveform is able to substantially enhance their heating ability. Interactions connect the heating performance of a system of nanoparticles to their concentration and spatial/orientational arrangement and can either increase[42,44,46] or decrease[43,44,46,48] the loss power of magnetic nanoparticles depending on nature and type of resulting particle aggregates and/or magnetic-moment orientations. The effect of interactions is usually not simulated in the rate equations framework[43,45–48].

After a brief overview of the model, Section III is devoted to study how non-harmonic driving field waveforms can produce hysteresis loops af greater area with respect to a harmonic excitation of same frequency and amplitude. In Section IV the effect of the Specific Loss Power arising from the studied waveforms is discussed considering the role of particle size, magnetic field amplitude and frequency. The special features of hysteresis loops produced by a square-wave field are studied in Section V, and a characteristic instability is pointed out and explained. Finally, in Section VI it will be shown how unconventional driving field waveforms can be made to comply with the requirement of keeping an acceptable level of living tissue heating.

II. DWS AND RATE EQUATIONS

Describing magnetic nanoparticles with predominant uniaxial anisotropy in terms of double-well systems (DWS) has notable advantages, as discussed elsewhere[33]. Rate equations are a most natural way to get an adequate picture of the behavior of a magnetic DWS submitted to a static or dynamical magnetic field, both at equilibrium and off-equilibrium[33,38]. In this paper, magnetic nanoparticles of size D and volume $V = (\pi/6)D^3$ are assumed to carry a magnetic moment $\mu = M_s V$ where M_s is the saturation magnetization of the material; when no magnetic field is applied the magnetic moment is aligned to the easy axis by uniaxial anisotropy of magnitude K_{eff}. In this work, the quasi-static blocking temperature $T_B = K_{eff}V/Lk_B$ is assumed to be below room temperature $T_R = 300$ K, so that the T_R/T_B ratio is always larger than unity. The quantity L is defined as $ln(\tau_0/\tau_{meas})$ where $\tau_0 \approx 10^{-9}$s is the pre-exponential factor of the standard Arrhenius formula[32] and $\tau_{meas} \simeq 100$ s is the measurement time in quasi-static conditions[41], so that $L \simeq 25.33$. In this paper, the following values of magnetic parameters, appropriate to magnetite nanoparticles around room temperature, will be used throughout: $M_s = 350$ emu/g (= 350 Am^2/kg); $K_{eff} = 2 \times 10^5$ erg/cm^3 (= 2×10^4 J/m^3).

The investigated magnetic DWS assemblies are made of monodisperse particles of size D whose easy directions are evenly distributed in space. For noninteracting nanoparticles, effects related to the presence of a continuous size distribution $p(D)$ can be quite naturally derived from our results.

Rate equations applied to an assemby of noninteracting magnetic DWS allow one to study the behavior of the occupancy numbers of the two energy wells as well as the global magnetization at all finite temperatures and under an arbitrary magnetic field[33].

The rate-equation approach is to be viewed as a simplifying approximation to the Fokker-Planck equation for the double-well problem[36,49]. The question arises where and when is this approximation viable. For magnetic nanoparticles, rate equations were shown[36] to naturally emerge from the Fokker-Planck equation when the ratio $K_{eff}V/k_BT$ is significantly larger than unity; therefore the validity of the approach at a given temperature depends on both magnetic anisotropy and nanoparticle size. With our K_{eff} value the condition is fulfilled (at and around room temperature) when $D \gtrsim 15$ nm; an increasingly less accurate approximation to the Fokker-Planck equation is expected with reducing the nanoparticle size

below about 15 nm. As a matter of fact, rate equations were successfully applied to study hysteretic effects in magnetic nanoparticles with values of the $K_{eff}V/k_BT$ ratio comparable to the ones we get when $D \gtrsim 15$ nm[30].

In the rate-equation approach, the redistribution of particles in the two wells of an assembly of DWS whose easy axes make an angle ϕ with the field direction is ruled by the equations:

$$\frac{dn_{1\phi}}{dt} = -\frac{1}{\tau_1(t)}n_{1\phi} + \frac{1}{\tau_2(t)}n_{2\phi} = \frac{1}{\tau_2(t)} - \left(\frac{1}{\tau_1(t)} + \frac{1}{\tau_2(t)}\right)n_{1\phi}$$
$$\frac{dn_{2\phi}}{dt} = \frac{1}{\tau_1(t)}n_{1\phi} - \frac{1}{\tau_2(t)}n_{2\phi} = \frac{1}{\tau_1(t)} - \left(\frac{1}{\tau_1(t)} + \frac{1}{\tau_2(t)}\right)n_{2\phi}.$$
(1)

The absolute occupancy numbers in the two wells are $N_{1\phi}$ and $N_{2\phi}$; their sum equals N_ϕ, the total number of DWS characterized by the angle ϕ. Here, the reduced quantities $n_{1\phi} = N_{1\phi}/N_\phi$ and $n_{2\phi} = N_{2\phi}/N_\phi$ are used ($n_{1\phi} + n_{2\phi} = 1$).

In the standard Arrhenius picture the escape frequencies appearing in Equations (1) are defined as $\tau_i^{-1} = \tau_0^{-1}exp\left[-(E_M - E_i)/k_BT\right]$ ($i = 1, 2$) where $E_i(t)$ are the energies of the two energy minima, $E_M(t)$ is the energy at the top of the barrier. The energies depend on time when $H = H(t)$. The problem's symmetry dictates the general relationship $\tau_1(-H) = \tau_2(H)$ that holds at all angles ϕ.

In rate equations containing time-dependent escape frequencies, detailed balancing is achieved only when $\omega\tau_c << 1$ where τ_c is the characteristic relaxation time of the system[50]. In magnetic nanoparticles, the free diffusion time of magnetization is[49]: $\tau_c = M_sV(1 + \alpha^2)/2\gamma\alpha k_BT$ where γ is the electron gyromagnetic ratio and α is the Gilbert's damping constant appropriate to describe intermediate-to-high damping ($\alpha \approx 1$)[30]. Using $\alpha = 0.5$ one gets $\tau_c = 1.06 \times 10^{-9}$ s for $D = 15$ nm. In this case, the driving-field frequency should be much lower than 1.50×10^8 Hz to guarantee detailed balancing. In fact, the driving-field frequencies used in this paper ensure that rate equations can be confidently applied for all studied nanoparticle sizes and all studied driving-field waveforms, as discussed in more detail in the Supplemental Material.

The double-well configuration depicted here is valid for $|H|$ values not larger than a maximum value $|H_{max}|$ that depends on angle ϕ (for $\phi = 0$ and $\phi = \pi/2$, $|H_{max}| = 2K_{eff}/M_s$).

Actually, when $|H| > |H_{max}|$ the DWS collapses and only one energy well is left.

When the system is submitted to a cyclic magnetization process under a harmonic magnetic field $H(t) = H_v cos(2\pi ft)$, where the maximum applied field H_v is referred to as the vertex field, the dimensionless rate equations (1) can be easily rewritten in terms of the dimensionless field $h = HM_s/2K_{eff}$.:

$$\frac{dn_{1,\phi}}{dh} = \mp\frac{1}{r(t)}\Big[\frac{1}{\tau_2(h)} - \Big(\frac{1}{\tau_1(h)} + \frac{1}{\tau_2(h)}\Big)n_{1,\phi}\Big]$$

$$\frac{dn_{2,\phi}}{dh} = \mp\frac{1}{r(t)}\Big[\frac{1}{\tau_1(h)} - \Big(\frac{1}{\tau_1(h)} + \frac{1}{\tau_2(h)}\Big)n_{2,\phi}\Big].$$

(2)

where the $\mp$ sign refers to the upper/lower loop branch, and the time-dependent sweep rate $r(t) = dh/dt = 2\pi h_v sin(2\pi ft)$ has been introduced. The dimensionless magnetic field $h = M_s H/2K_{eff}$ is the independent variable, $n_{1\phi}$ and $n_{2\phi}$ are the reduced occupancy numbers in the two wells ($n_{1\phi} + n_{2\phi} = 1$), the suffix ϕ indicating the angle between easy axis and magnetic field.

Equations 2 can be numerically solved using the time-dependent rate $r(t)$; in the existing literature however[38,51], these are usually further simplified at all driving-field frequencies by introducing a constant (r.m.s.) sweep rate, defined as $r_{RMS} = (\pi/\sqrt{2})h_v f$ where h_v is the dimensionless vertex field, so that h is assumed to change from the upper vertex (h_v) to the lower vertex ($-h_v$) and viceversa according to the linear law $h(t) = \mp h_v \pm r_{RMS}t$. Basically, this corresponds to assimilate a harmonic driving field at frequency f to a Symmetric Triangular (ST) waveform. In the following, the same approximation (i.e., $r(t) \rightarrow r_{RMS}$ in Equation 2) will be used for all studied waveforms.

In magnetic hyperthermia, the efficiency of heat generation from a nanoparticle is related to the Specific Loss Power (SLP); considering magnetic losses only, $SLP = A_L f$ where A_L is the hysteresis loop's area per unit mass and f the driving field frequency; an obvious way to increase the SLP is to increase f (within the safety limits imposed by physiological restrictions[52,53]). The question arises whether it is possible to substantially increase the SLP of a nanoparticle treated as a DWS by modifying the shape of the driving-field waveform.

III. DRIVING-FIELD WAVEFORMS: A STRATEGY TO ENHANCE THE SLP

The shape of a harmonic waveform (treated as a ST wave) ca be made to naturally evolve into an Asymmetric Triangular (AT) waveform, or into a Square Wave (SQ). A detailed analysis of the effects of both driving-field waveforms on a magnetic DWS on the SLP is reported below. Magnetic nanoparticles are assumed to be made of magnetite (Fe_3O_4) with size in the interval 11-22 nm and to have no translational nor rotational degrees of freedom so that the only heat generation mechanism is by Néel's relaxation[28]; all effects are studied at room temperature (T_R). Our assumptions are substantiated by the following arguments: a) nanoparticle composition and size range comply with the prescriptions by U.S. Drug and Food Administration[54] and correspond to superparamagnetic nanomaterials actually investigated *in vivo*[7,21]; b) in real cases, nanoparticles injected in suspension in a living body often anchor to target tissues so that their ability to rotate their crystallographic axes in space is greatly reduced (this happens, e.g., to particles subjected to immobilization in a cellular environment[55,56]).

It should be noted that a small change in D entails a much larger change in the T_R/T_B ratio, so that particles of different size in a polydisperse system may give largely dissimilar contributions to the SLP because of their different magnetic state. This is clearly true for nanoparticles submitted to a harmonic driving field. We shall show, however, that strict size monodispersity is not mandatory when other driving field waveforms are exploited.

III.1. Asymmetric Triangular Waveform

The AT wave parameters are shown in Figure 1 (left panel). The asymmetry is defined by the dimensionless quantity x ($0 < x \leq 0.5$, the upper limit corresponding to the ST wave). When $x \to 0$ the AT wave becomes an ideal sawtooth wave. In this case, the absolute value of the sweep rate is very different between lower ($-h_v \to +h_v$) and upper ($+h_v \to -h_v$) hysteresis loop's branches, with $r_{LO} < r_{UP}$. The resulting effect on the loop's shape is shown in Figure 1 (right panel) for a 15-nm particle with $\phi = \pi/4$, $f = 100$ kHz and $h_v = 0.2625$ (corresponding to a vertex field of 300 Oe $\simeq$ 23.9 kA/m). A qualitatively similar behavior is observed for all ϕ angles.

With decreasing x the upper branch of the loop becomes much larger than the lower
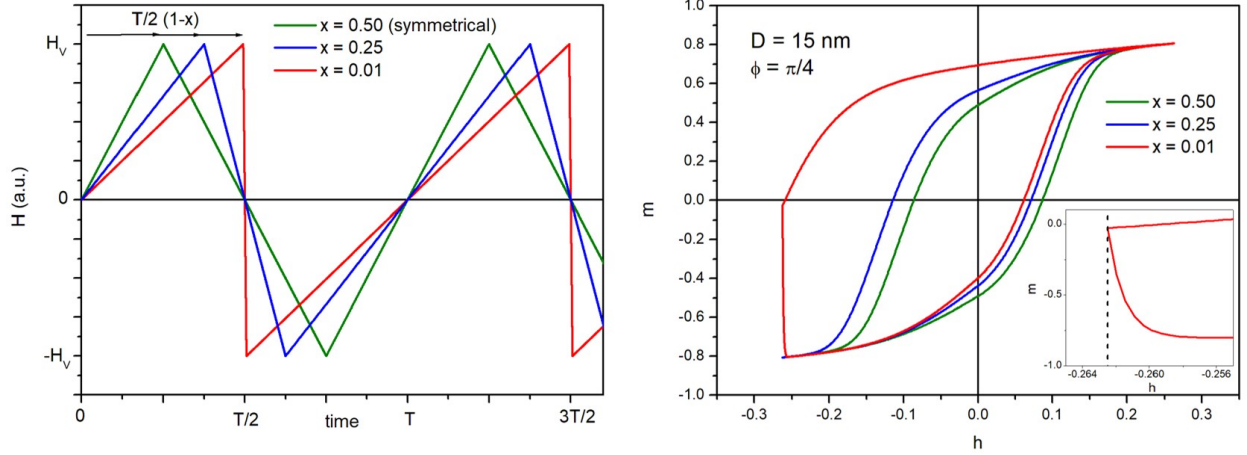
FIG. 1. Left panel: parameters defining the Asymmetric Triangular Waveform. Right panel: hysteresis loops of collinear ($\phi = \pi/4$) monodisperse nanoparticles ($D = 15$ nm) for three values of the asymmetry parameter x. Inset: detail of the region around the negative vertex field for a sawtooth wave, $x = 0.01$.

one and the coercive field becomes highly asymmetric with an apparent increase of the loop's area. In the nearly vertical portion of the loop observed around $-h_v$ for $x = 0.01$ the occupancey numbers suddenly change ($n_{1,\phi} \to 0, n_{2,\phi} \to 1$). This effect occurs when the absolute value of the sweep rate switches from very high to low, i.e., exactly at the beginning of the lower loop's branch. In fact, for a true sawtooth waveform, the occupancy numbers $n_{1,\phi}, n_{2,\phi}$ virtually do not change when the field decreases from $+h_v$ to $-h_v$ because of the very high sweep rate (the upper branch therefore corresponds to a nearly-adiabatic transformation for the DWS). In such a way, a highly off-equilibrium condition of both occupancy numbers around $-h_v$ is achieved; in particular, $n_{1,\phi}(-h_v) >> n_{2,\phi}(-h_v)$ whilst at equilibrium the relationship would be reversed. When the sweep rate is abruptly reduced, the system has enough time to relax towards equilibrium. The inset of Figure 1 (right panel) shows in detail how the system reaches the new steady-state condition on the lower loop's branch.
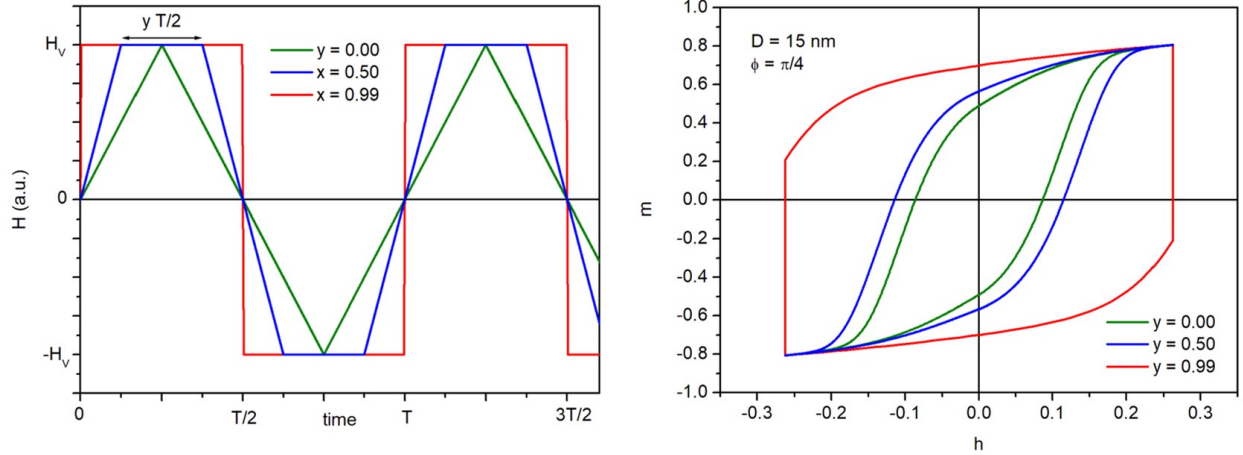
FIG. 2. Left panel: parameters defining the Trapezoidal/Square Waveform. Right panel: hysteresis loops of collinear ($\phi = \pi/4$) monodisperse nanoparticles ($D = 15$ nm) for three values of the parameter y.

III.2.   Trapezoidal / Square Waveforms

The trapezoidal waveform's parameters are shown in Figure 2 (left panel). The dimensionless quantity y ($0 \leq y < 1$) defines the time interval $yT/2$ during which the field remains fixed at the positive/negative vertex value; the ST wave corresponds to the case $y = 0$. The ideal square wave (SQ) is a limiting case of the trapezoidal waveform ($y \rightarrow 1$).

In a trapezoidal wave, the field sweep rate is the same (in absolute value) for the two loop's branches; on the contrary, the vertex field is applied to the DWS during the time $yT/2$. In the SQ-wave limit, this time approaches $T/2$ and the sweep rate becomes very high. The resulting effect on the loop's shape is shown in Figure 2 (right panel) for a 15-nm particle using the same parameters as in the AT case. With increasing y, the loop becomes increasingly larger with symmetric coercive fields; the loop's area is strongly enhanced. For a nearly-ideal SQ wave ($y = 0.99$), the hysteresis loop becomes a rectanguloid composed of two branches (from $+h_v$ to $-h_v$ and viceversa) corresponding to the paths followed by the system by effect of the high sweep rate (nearly-adiabatic in nature according to our previous considerations) and of two vertical segments corresponding to the relaxation of the magnetization towards equilibrium at constant field ($h = \pm h_v$). It should be noted that a SQ-wave driving field is inherently different from the standard case of a continuous-wave
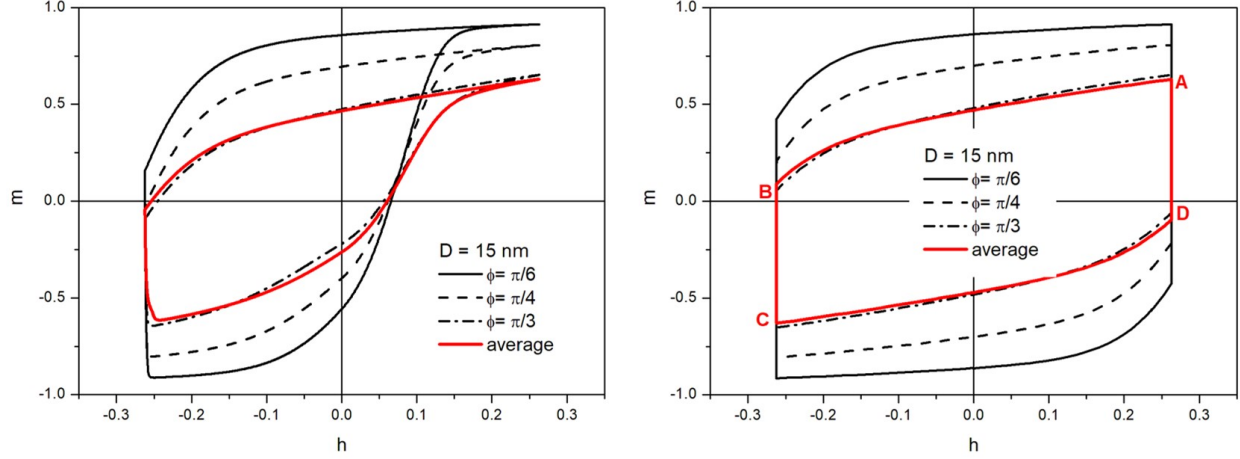
10

FIG. 3. Left panel: hysteresis loops of collinear monodisperse nanoparticles ($D = 15$ nm) submitted to an AT wave ($x = 0.01$) for three values of angle ϕ; the loop of an assembly of nanoparticles with random easy axis directions is shown as a red line. Right panel: the same as in the left panel for 15 nm nanoparticles submitted to a SQ wave with $y = 0.99$.

driving field, because the DWS is submitted to a *constant* field for a time very close to $T = 1/f$. In spite of this, a large amount of energy is transferred from the DWS to the environment during each full cycle. A detailed analysis of this special case is done in Section V.

The effect of changing the angle ϕ on the shape of both sawtooth-wave and SQ-wave driving fields is shown in Figure 3 for 15-nm nanoparticles at the frequency $f = 100$ kHz. The loop area steadily decreases with increasing ϕ, and disappears for $\phi = \pi/2$, as expected[57]. The average over a random distribution of easy axes directions in 3D is also reported in Figure 3. In three dimensions, the average of a ϕ-dependent quantity $g(\phi)$ is $\sum_1^N g(\phi_i) sin(\phi_i) / \sum_1^N sin(\phi_i)$ where the sum extends over N angles in the interval $-\pi/2 \leq \phi_i \leq \pi/2$. Computationally stable results are obtained putting $N = 181$. The general features of both loops appear to be preserved by the averaging procedure; in particular, the SQ wave still gives rise to a loop with rectanguloid shape (labeled as $ABCD$ in Figure 3).

In the following Sections, all results will refer to properties of a DWS assembly with randomly distributed easy axes.

11

IV. INFLUENCE OF DRIVING-FIELD WAVEFORM ON THE SLP

Rate equations allow one to study the effect of the driving-field waveform on the SLP of an assembly of monodisperse nanoparticles. The SLP, defined as the product $A_L f$ (where A_L is the loop's area per gram of magnetic material) is studied at room temperature considering nanoparticle diameters in the range 11-22 nm, vertex fields up to 23.9 kA/m (corresponding to $|h_v| \leq 0.2625$) and frequencies in the range $10 - 500$ kHz. These intervals closely match the operating conditions for present-day systems for magnetic hyperthermia[58]. It should be reminded that the SLP is not an intrinsic property of a nanoparticle system because it is strongly dependent on specific treatment conditions (frequency and magnetic field amplitude).

IV.1. Effect of Nanoparticle Size

The behavior of the SLP as a function of particle size D is reported in the left panel of Figure 4 for all studied driving-field waveforms at fixed frequency and $h_v = 0.2625$. The curve for the ST wave also represents the effect of a harmonic driving field when the r.m.s. sweep rate is used. The common feature of the three curves is the presence of a maximum of SLP at intermediate D values. The driving-field frequency being constant, the SLP behavior reflects changes in the loop's area. For small D values the SLP is low because the operating temperature is much above the blocking temperature of these particles, whose hysteresis loops merely correspond to a slight broadening of the equilibrium curve sustained by the high-frequency driving field; on the other hand, in large nanoparticles the vertex field becomes smaller than the coercive field and the loop's area decreases again (see the Supplemental Material). It is worth noting that the rate Equations 2 become increasingly less accurate when $D \lesssim 15$ nm, as discussed previously; this is indicated by the dotted lines in Figure 4

In the ST case, the SLP maximum is particularly narrow. Such a circumstance has already been noted[48] and is quite detrimental to the practical use of real nanoparticle suspensions where some size polydispersity is present. In the AT case, the SLP maximum becomes broader towards the low-D region, an effect which can be understood in the following way: on the nearly-adiabatic branch of the loop the magnetic moments of small nanoparticles have
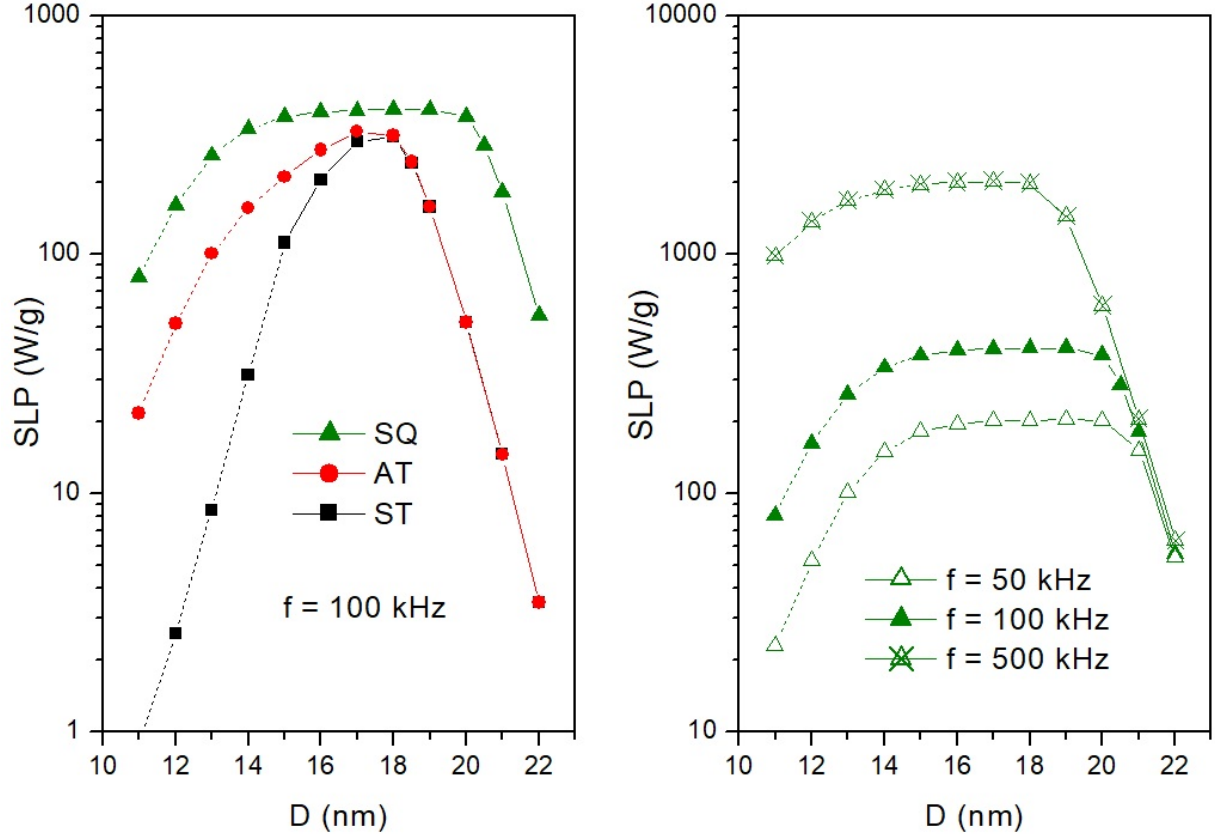
12

FIG. 4. Left panel: effect of particle size D on the SLP released by a random assembly of monodisperse magnetite nanoparticles for three applied-field waveforms (triangular symmetric, triangular asymmetric, square) of same frequency and amplitude. Right panel: SLP vs. D curves for a SQ wave at three excitation frequencies. Dotted lines indicate the region where rate equations become gradually less accurate.

not enough time to redistribute between wells, so that they behave as virtually blocked; the magnetization is far from equilibrium and the loop's area large; on the contrary, on the slower branch of the loop - as well as on *both* branches of a loop generated by the ST wave - the occupancy numbers and the magnetization are close to equilibrium, which implies a narrow hysteresis loop.

However, the best performance of the DWS assembly is when a SQ-wave driving field is applied: the SLP maximum becomes not only higher but also considerably broader, with a plateau extending from 15 to 20 nm. This is an important improvement because the need of using a perfectly monodisperse nanoparticle suspension is largely reduced. As an example,

supposing that the nanoparticle are distributed according to a gaussian centered at $D = 17.5$ nm with standard deviation $\sigma = 2$ nm, the average SLP amounts to 198.5 W/g in the ST case, 227.1 W/g in the AT case, 371.4 W/g for a SQ driving field.

The broadening of the SLP maximum has two different origins: the plateau extends towards the low-D region for the same reasons as in the AT case, with even higher efficiency because now each loop hosts two nearly-adiabatic branches; on the contrary, the broadening towards the high-D region arises from the specific features of the SQ-wave hysteresis loops, which will be discussed in detail in Section V.

The SLP plateau is observed at all significant driving-field frequencies, as shown in Figure 4 (right panel) where it is observed to slightly drift towards left and to become slightly narrower with increasing f. With the considered magnetic parameters, the optimum SLP condition occurs when D is in the 15-18 nm range at all frequencies.

IV.2. Effect of Vertex Field

The behavior of the SLP as a function of vertex field is shown in Figure 5 for a random DWS assembly with $D = 15$ nm and $f = 100$ kHz; the value of D has been selected to enhance the difference between the three waveforms. The SLP monotonically increases with vertex field, as expected; the slope is significantly higher in the SQ-wave case. With the maximum field amplitude of Figure 5, the $H_v f$ product is between the two typical limits proposed in the literature[52,53] at this working frequency. Most of the *in vivo* experiments are done using $H_v f$ products precisely in this range. The behavior of SLP vs. H_v is basically independent of particle size.

IV.3. Effect of Frequency

The effect of frequency on the energy loss per cycle ($\equiv A_L$) and the SLP is shown in the left panels of Figure 6 for all studied waveforms. The considered D values are in the range 12-21 nm and the vertex field is fixed at $H_v = 300$ Oe (23.9 kA/m). Results for $D = 12$ nm are pictured by dotted lines to remark that rate equation are less accurate for this nanoparticle size.

For a ST-wave driving field (first row), the frequency behavior of the energy loss is strongly
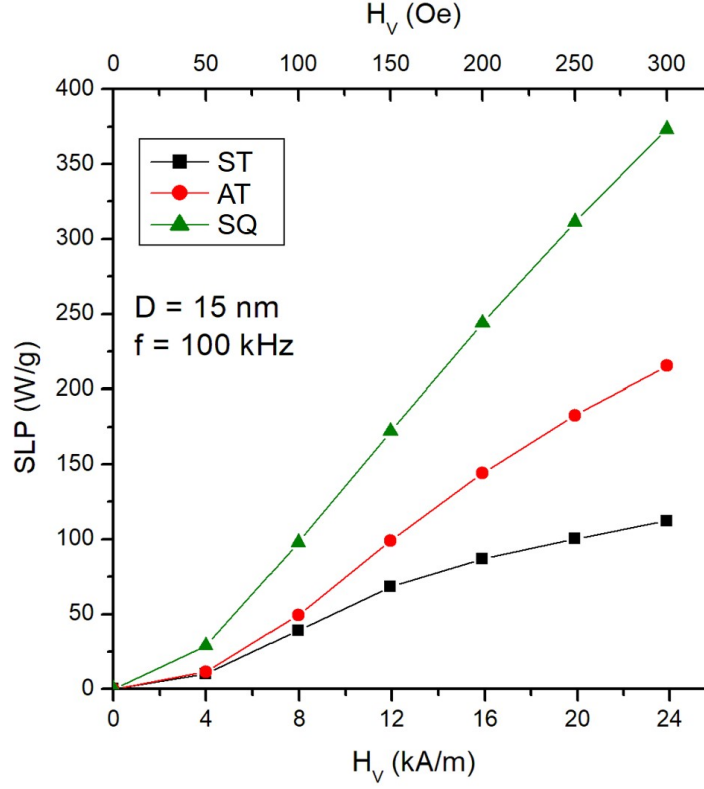
14

FIG. 5. SLP released by a random assembly of monodisperse magnetite nanoparticles ($D = 15$ nm) as a function of vertex field for three applied-field waveforms (triangular symmetric, triangular asymmetric, square).

influenced by D, ranging from a linear increase ($A_L \sim f$) when $D = 12$ nm to a hyperbolic decrease ($A_L \sim 1/f$) when $D = 21$ nm; for intermediate diameters a maximum ($D = 18$ nm) or a tendency towards a maximum ($D = 15$ nm) are observed. Linear response theory[59] predicts a dependence of A_L as f in small nanoparticles and as $1/f$ in large nanoparticles with an intermediate maximum, exactly as observed here. Actually, linear response theory cannot be directly applied to our curves because the condition of direct proportionality between m and h is not fulfilled; however, the observed behavior is somewhat reminiscent of that result.

For AT-wave and SQ-wave driving fields (second and third row in Figure 6, respectively) a similar general behavior of $A_L(f)$ for different D values is observed; the curves reflect the complex interplay between particle size, frequency and applied waveform (represented, e.g., by the behavior reported in Figure 4); in particular, no linear dependence of A_L on f is
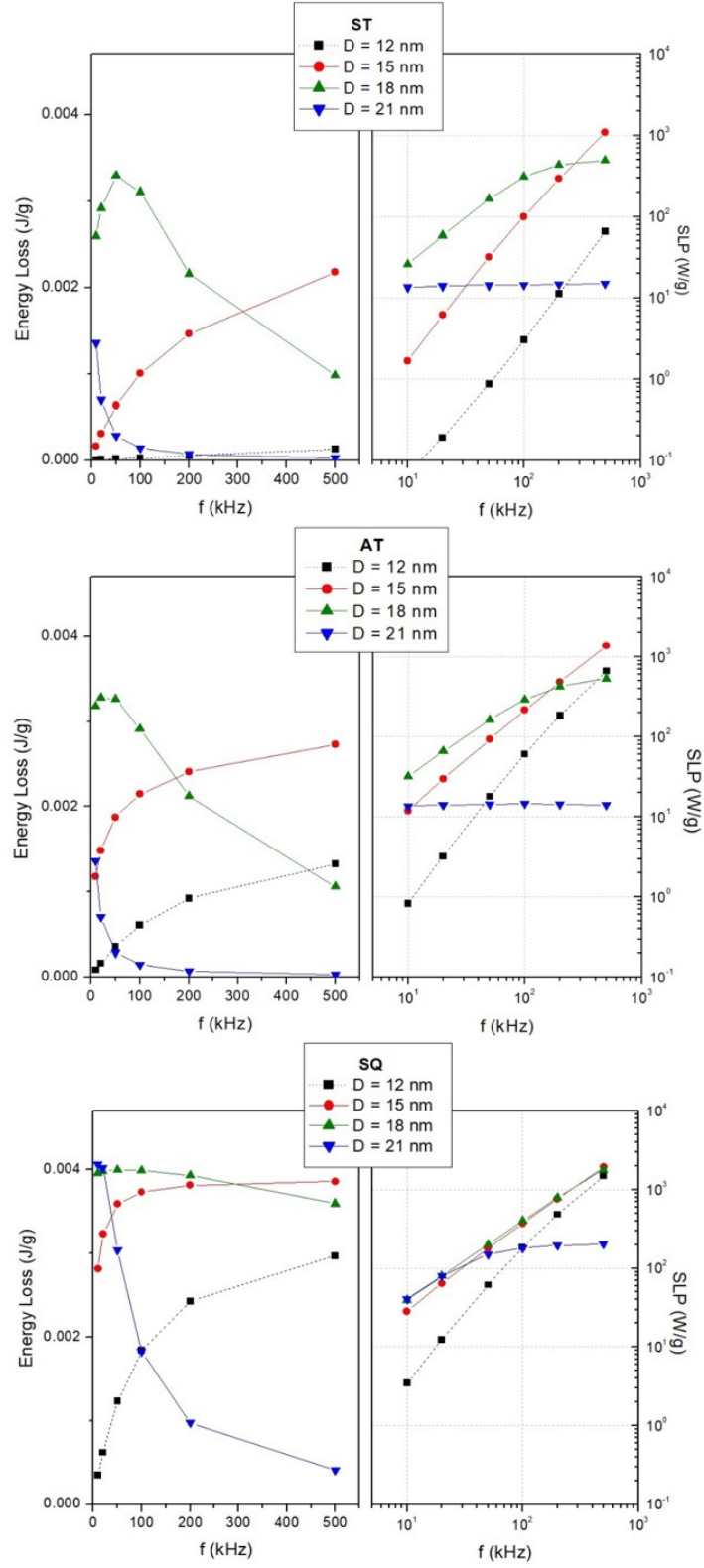
FIG. 6. Energy loss and associated SLP (left and right panels, respectively) as functions of frequency for different nanoparticle sizes and different driving field waveforms.

observed, even for the smallest particles.

The corresponding SLP curves (right panels) show that the driving-field waveform has notable practical effects on this quantity. When a ST-wave driving field is used (first row), only particles with $D \leq 15$ nm give a SLP which increases with increasing frequency; the SLP of larger particles is or becomes saturated in the studied frequency range ($D = 21$ and $D = 28$ nm, respectively).

The situation is basically the same in the case of the AT-wave driving field (second row) but for an increase of the SLP at all frequencies, the effect being particularly marked in $D = 12$ nm particles. On the other hand, the SQ-wave driving field (third row) is able to inhibit the saturating trend of $A_L(f)$ for $D = 18$ nm and to strongly increase the SLP associated to the $D = 21$ nm particles (even if the saturating behavior is not suppressed at high frequency). Moreover, the SLP of all particles below 18 nm become of the order of 2×10^3 W/g at the upper limit of the investigated frequencies.

The present results clearly show how important is a correct choice of parameters (both intrinsic such as particle composition, diameter, shape and extrinsic such as driving field frequency, intensity, shape) in order to optimize the SLP for hyperthermia applications.

V. SPECIAL FEATURES OF LOOPS DRIVEN BY A SQUARE-WAVE FIELD

Hysteresis loops of an assembly of magnetic DWS submitted to a SQ-wave driving field radically differ from the ones driven by continuous-wave fields because of the presence of two segments where the magnetization is allowed to naturally relax towards the equlibrium condition at constant field and temperature. In this case the time spent by the system at constant field dominates over the time taken by the field to reverse from positive to negative vertex and viceversa.

The SQ-wave loop of Figure 2 ($D = 15$ nm, $\phi = \pi/4$, $y = 0.99$) is reported in Figure 7 as an example. The magnetization loop in the (h, m) plane is comprised of two nearly-adiabatic branches ($A_\phi \rightarrow B_\phi$, $C_\phi \rightarrow D_\phi$) connected by two vertical segments ($B_\phi \rightarrow C_\phi$, $D_\phi \rightarrow A_\phi$). On each nearly-adiabatic branch (e.g., $A_\phi \rightarrow B_\phi$) the DWS go off equilibrium because the magnetic-field change is so fast that the occupancy numbers in each of the two wells have almost no time to rearrange in response to the evolution of magnetic field $h(t)$; as a consequence, there is almost no release of energy from each DWS to the surroundings and
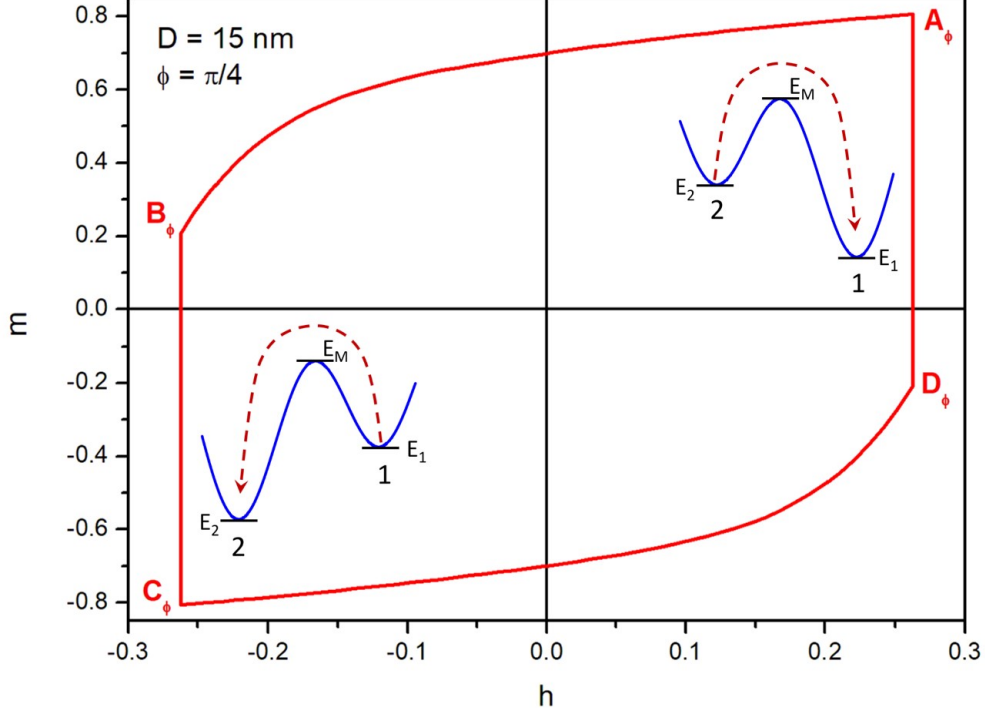
17

FIG. 7. Typical hysteresis loop under SQ-wave applied field for collinear particles with $\phi = \pi/4$. Loop vertexes are labelled according to the text. Particle redistribution between wells at negative and positive vertex field is schematically represented.

a large potential energy is accumulated in the magnetic system; on the contrary, on each vertical segment (such as $B_\phi \to C_\phi$) the DWS relax towards equilibrium and the accumulated energy is released to the environment.

Let us call t_0 the time at which the system reaches vertex B_ϕ after describing the upper nearly-adiabatic loop branch $A_\phi \to B_\phi$. As already pointed out, in B_ϕ the occupancy numbers $n_{1\phi}$ and $n_{2\phi}$ are far from equilibrium, being close to the equilibrium values at vertex A_ϕ instead. Therefore, the well higher in energy (n. 1 in the left-side sketch of Figure 7) is still almost completely full, and well 2 almost completely empty; during relaxation ($t > t_0$) well 1 is emptied in favor of well 2 according to the time-dependent rate equation (see the Supplemental Material):

$$\frac{dn_{1\phi}}{dt} = \frac{1}{\tau_2(t)} - \left(\frac{1}{\tau_1(t)} + \frac{1}{\tau_2(t)}\right)n_{1\phi} \simeq -\frac{1}{\tau_1(t)}n_{1\phi}, \tag{3}$$

18

where $\tau_i = \tau_0 e^{(E_M - E_i)/k_B T}$ and $T = 300$ K. Here, $E_M(t)$ is the energy at the top of the barrier and $E_i(t)$ are the energies of the DWS minima. For $h = -h_v$, $E_1 > E_2$ (see Figure 7 for an explanation of symbols). The simplifying approximation in Equation 3 is possible because the term $1/\tau_2$ can be easily shown to be negligible in this case. As a consequence, $n_{1\phi}$ exponentially relaxes towards equilibrium according to the law:

$$n_{1\phi}(t) = [n_{1\phi}(t_0) - n_{1\phi}(\infty)]e^{-(t-t_0)/\tau_1} + n_{1\phi}(\infty) \simeq n_{1\phi}(t_0)e^{-(t-t_0)/\tau_1} \qquad (t \geq t_0)$$

because at equilibrium $n_{1\phi}(\infty) \simeq 0$ at $h = -h_v$. The time constant is:

$$\tau_1 = \tau_0 e^{(E_M - E_1)/k_B T} \qquad (4)$$

and depends on angle ϕ through $E_M(\phi), E_1(\phi)$. The problem's simmetry implies that: a) the time constants for relaxation are the same at both positive and negative vertex field with the trivial interchange $1 \leftrightarrow 2$; b) the minimum of $\tau_1(\phi), \tau_2(\phi)$ occurs for $\phi = \pi/4$. Let us call $\tau_{1,2}(\phi = \pi/4) = \tau_{rel}$. Such a quantity should be compared with the time $yT/2$ during which the magnetic field remains fixed at the vertex value (see Figure 2). If $\tau_{rel} << yT/2$, the system has enough time to reach equilibrium; otherwise relaxation towards equilibrium is incomplete. A threshold condition for the SQ-wave frequency is easily obtained by requiring that $yT/2 = y/2f$ be larger than $5\,\tau_{rel}$. Note that if this condition is fulfilled for $\phi = \pi/4$ it is automatically fulfilled for all ϕ angles. The threshold frequency is:

$$f_{thr} = \frac{y}{10}\frac{1}{\tau_{rel}} = \frac{y}{10\tau_0}e^{-(E_M - E_m)_{(\pi/4)}/k_B T} \qquad (5)$$

where for a SQ wave $y \simeq 0.99$ and E_m is the common value of $E_1(-h_v)$ and $E_2(+h_v)$. The system reaches equilibrium on both vertical segments only if $f < f_{thr}$.

The behavior of f_{thr} as a function of h_v is shown in the left panel of Figure 8 for four values of D. Horizontal full symbols indicate loops with different vertex fields done at fixed frequency ($f = 500$ kHz). Considering, for example, 15-nm nanoparticles, three representative points ($H_v \leq 150$ Oe) are above the corresponding threshold line, the remaining three being below. The validity of Equation 5 is verified in the middle panel, where all four vertexes of the three inner loops are not on the equilibrium curve (dashed sigmoidal line), indicating
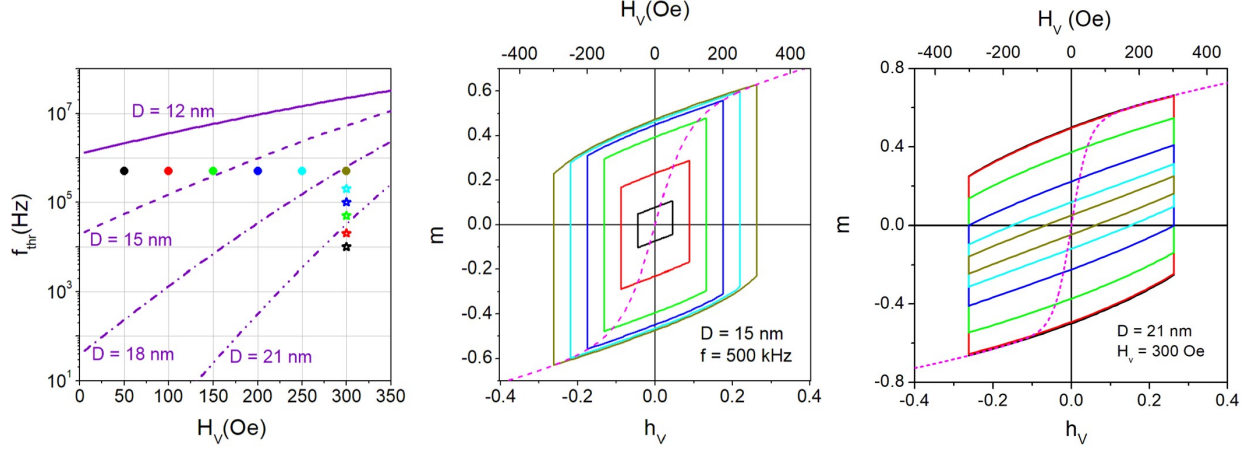
19

FIG. 8. Left panel: frequency threshold lines for the relaxation of magnetization towards equilibrium at constant field for different particle sizes. Full relaxation occurs for all representative points lying below each line. Middle panel: hysteresis loops of 15 nm nanoparticles as functions of vertex field at fixed frequency; line colors correspond to the representative points shown in the left panel (horizontal set). Right panel: hysteresis loops of 21 nm nanoparticles as functions of frequency at fixed vertex field; line colors correspond to the representative points shown in the left panel (vertical set).

incomplete relaxation along the vertical segments, whereas two vertexes of the larger loops are on the equilibrium magnetization curve, indicating full relaxation.

On the other hand, vertical open symbols in Figure 8 correspond to loops done at different frequencies and same vertex field, $H_v = 300$ Oe (23.8 kA/m). Considering, for example, 21-nm nanoparticles, only two representative symbols at low magnetizing frequencies are below the threshold line; therefore, only these loops are predicted to have two vertexes on the equilibrium magnetization curve, as actually verified in the right panel. With increasing f, 21-nm nanoparticles become increasingly unable to reach equilibrium on the vertical segments, and the loop area becomes increasingly smaller.

The behavior highlighted in Figure 8 explains the behavior of the SLP plateau of Figure 4 for large D values. The area starts reducing when the threshold frequency (which is a decresing function of D) shifts below the driving-field frequency; the lower f_{thr} is, the smaller the area. Therefore in practical applications of SQ-wave excitation it is important that the driving-field frequency be adjusted according to the dominant D value of the exploited

20

nanoparticle system, or viceversa that the nanoparticles be chosen to match the available driving field frequency.

Another important point is about loop's stability. Let us suppose that the cyclic magnetization process is turned on starting from the ideally demagnetized state (an example is given in the left panel of Figure 9): the initial point in the (h, m) plane is $(0, 0)$; the DWS assembly reaches point F on the first magnetization curve; then, the system freely relaxes towards point A; thereafter, the loop proper begins $(A \rightarrow B \rightarrow C \rightarrow D \rightarrow A)$. Now, it is observed that when point A is on the equilibrium magnetization curve, as in the left panel, all ensuing loops are perfectly stable in time. This means that the $(A \rightarrow B \rightarrow C \rightarrow D \rightarrow A)$ path is always the same. In particular, the upper and lower remanences m_{RUP} and m_{RLO} have the same absolute value, so that their arithmetic mean is zero. However, when point A is *not* on the equilibrium magnetization curve, the ensuing loops are instable, as shown in the right panel of Figure 9. Initially, the trajectories of instable loops do not close on themselves and magnetization keeps spiralling in the (h, m) plane; the arithmetic mean of the two remanences starts from a positive value and becomes zero only after an ideally infinite number of iterations; in other words, the system is self-adjusting and the spiral path initially followed by the magnetization in the (h, m) plane finally transforms into a closed loop. The ability to reach the steady state depends on driving-field frequency. The effect occurs for all values of angle ϕ; however, it can be more easily explained when $\phi = 0$, as shown in the Appendix.

Therefore, SQ-wave loops characterized by incomplete relaxation on the vertical segments should be avoided not only because the associated area is definitely smaller but also because of the inherent instability of the response of the system. Increasing the driving-field frequency in order to enhance the SLP can lead one to break the threshold f_{thr} with detrimental consequences on the efficiency of a nanoparticle system for hyperthermia applications.

VI.   DETRIMENTAL EFFECTS ON LIVING TISSUES

Trapezoidal/square and triangular asymmetric magnetic field waveforms allow higher SLP values to be attained in comparison to harmonic or triangular symmetric waveforms of same frequency and amplitude. Although the present results are primarily intended as a guidance to build laboratory demonstrators and devise *in vitro* experiments, some details will require
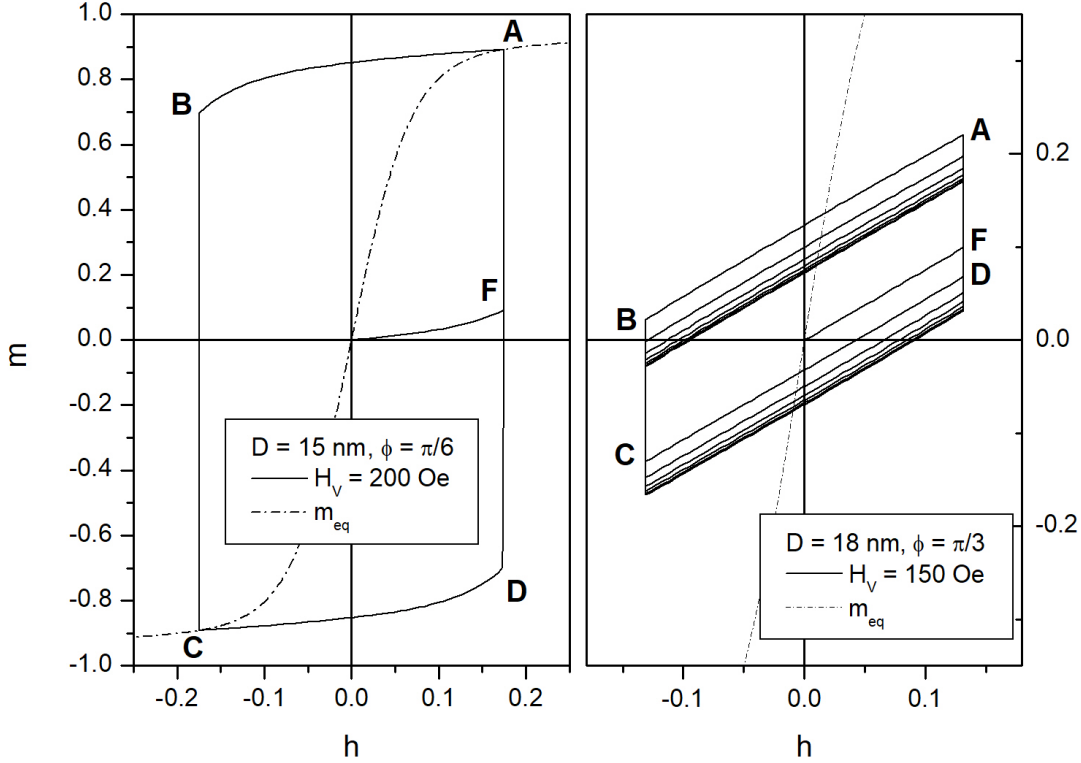
FIG. 9. Left panel: stable hysteresis loop for collinear monodisperse nanoparticles with $\phi = \pi/6$; vertex A is on the equilibrium magnetization curve (shown as a dotted-dashed line). Right panel: unstable loop for collinear monodisperse nanoparticles with $\phi = \pi/3$; vertex A is far away from the equilibrium magnetization curve (shown as a dotted line).

particular attention when *in vivo* experiments and applications will be envisaged.

As known, the applied field exploited to generate localized heat by Néel relaxation in nanoparticles also has undesired effects on the whole of the body crossed by the magnetic flux lines. In the high-frequency region considered in this paper, two detrimental effects related to the eddy-current density $j(r,t)$ should be considered: stimulation of cardiac muscle and nerve fibers[60] and healthy tissue heating. Both effects need to be kept under control[52,53,61]. A detailed calculation of the eddy-current density flowing in a body submitted to a periodic waveform is reported in the Supplemental Material, where it is shown that using non-harmonic waveforms still complies with the requirement of not introducing damage to living bodies or major discomfort to patients.

Here, the eddy-current effect of a generic trapezoidal wave ($0 < y < 1$) is compared to the one of a triangular symmetric wave ($y = 0$). The space- and time-averaged electrical power (per unit mass) released by the eddy currents induced by a periodic magnetic field in the cylindric body of radius r_{max} is $SLP_{SYMM} = \bar{\sigma}\bar{E}^2/\rho$, where $\bar{E}$ is the mean induced electrical field, $\bar{\sigma}$ is the conductivity and ρ the mass density of living tissues at the frequency f; for a harmonic waveform ($H(t) = H_V cos(2\pi ft)$) an elementary calculation[52] shows that $SLP_{HAR} = \bar{\sigma}\mu_0^2 H_V^2 f^2 r_{max}^2/\rho$. For a triangular symmetric waveform it can be easily shown that this quantity becomes $SLP_{TS} = 2\bar{\sigma}\mu_0^2 H_V^2 f^2 r_{max}^2/\rho$.

On the other hand, for a trapezoidal waveform the magnetic field is constant during most of time, reversing its sign once per half period. As a consequence, in a dielectric body the absolute value of the induced emf on a circumference of radius r is $|dB_\Phi/dt| \simeq \pi r^2 \mu_0 dH/dt$ during reversal and is equal to zero for the remaining time. In this case, $dH/dt = 2H_v/[(1-y)T/2] = 4H_v f/(1-y)$; such a quantity can become very large when $y \to 1$. The electrical field on the same circumference is $E(r) = 2\mu_0 r H_v f/(1-y)$, and the expression for the space- and time averaged power for a trapezoidal waveform with $y < 1$ becomes:

$$SLP_{TRAP} = \frac{2\sigma}{\rho(1-y)}\mu_0^2 H_V^2 f^2 r_{max}^2$$

In this case the power is relased in bursts, the time-averaged power being equal to the peak power multiplied by the duty cicle $(1-y)$. The condition for dealing with a trapezoidal wave which generates in the living tissues the same eddy-current SLP as a triangular symmetric or harmonic wave (of same frequency and amplitude) does, is:

$$\left(H_v f r_{max}\right)_{TRAP} = \sqrt{1-y}\left(H_v f r_{max}\right)_{TS} = \sqrt{\frac{1-y}{2}}\left(H_v f r_{Max}\right)_{HAR}$$

As a consequence, it appears possible to exploit a high-performance trapezoidal/square waveform whilst maintaining the same safety level of a harmonic waveform by suitably acting on the four variables y, H_V, f, r_{max}.

CONCLUDING REMARKS

Rate equations applied to magnetic nanoparticles help study their hysteretic properties under a cyclic driving field at frequencies suitable for magnetic hyperthermia treatments. Although rate equations are just an approximation to real magnetization dynamics in nanoparticles, the resulting picture is sufficiently accurate and can be gained without much computational effort. The present results, limited to noninteracting particles, are intended to serve as a starting point for future studies where the effect of interactions is switched on.

We have shown that changing the waveform of the driving field has considerable effects on the Specific Loss Power arising from Néel relaxation of an assembly of nanoparticles with randomly distributed easy-axes directions. In particular, using a sawtooth or a trapezoidal/square driving field waveform provides substantial advantages with respect to dealing with a harmonic or triangular symmetric waveform of same frequency and amplitude.

Among the explored cases, the trapezoidal/square waveform seems to be particularly promising for two orders of reasons: a stronger enhancement of the SLP is achieved and the range of nanoparticle sizes useful to produce an optimal SLP becomes much wider, allowing one to take advantage of both features in magnetic hyperthermia applications. Actually, some requirements should be addressed when using this driving-field waveform: a suitable feed circuit is needed to generate trapezoidal/square waves of electrical current in the magnetizing coil(s) at the right frequencies and amplitudes; hysteresis loop instability (Section V) is to be avoided, so that field amplitude and/or frequency need to be tuned taking into account nanoparticle size; finally, physiological restrictions to therapeutic use need to be properly considered, as discussed in Section VI. Nevertheless, these requirements can be technically fulfilled.

In conclusion, the choice of a specific waveform may result in a substantial enhancement of the heating power of magnetic nanoparticles. Generally speaking, the shape of the driving-field waveform should be viewed as an additional tunable parameter for achieving an optimal SLP, and should be considered not of lesser importance than nanoparticle composition and size, or frequency and amplitude of the excitation.
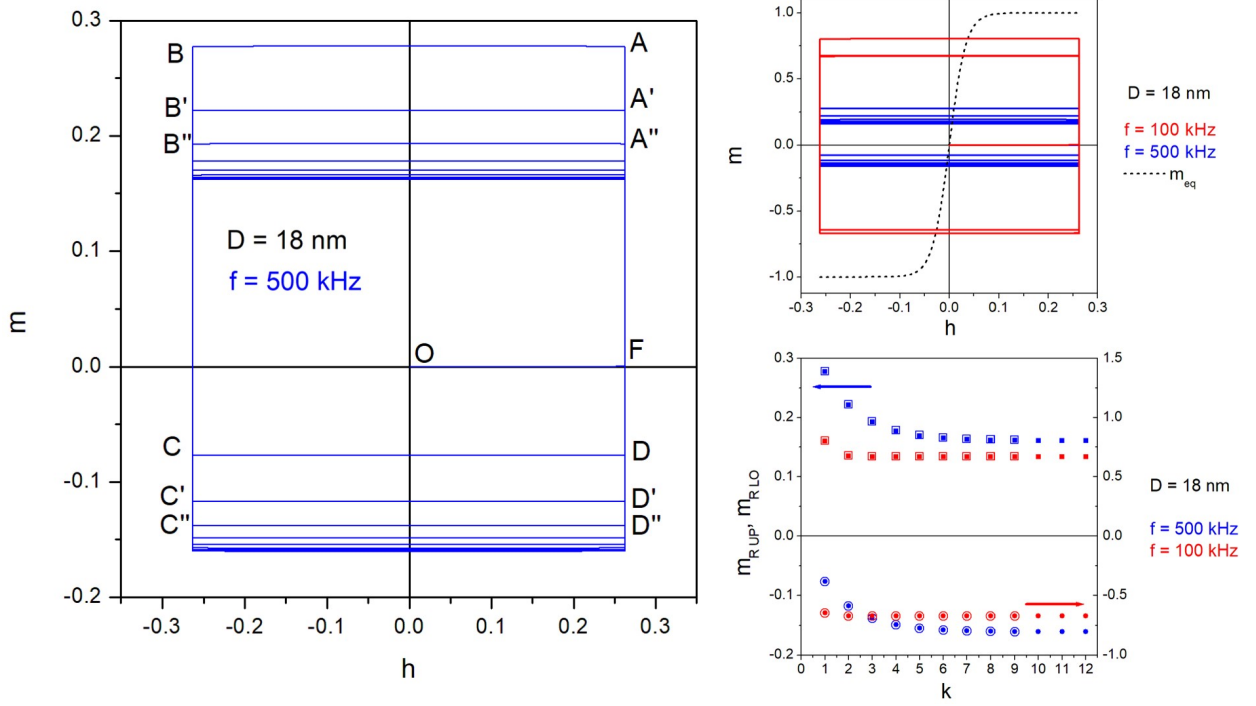
FIG. 10. Left panel: rectangular unstable loop for $\phi = 0$. Labels indicate successive vertex points (see text for details). Right upper panel: two unstable rectangular loops characterized by incomplete relaxation towards equilibrium (the equilibrium curve is shown as a dotted line). Right bottom panel: resulting positive and negative remanences as functions of index k (full symbols: approximate model, Equations (A.1) and (A.2); open symbols: exact numerical solution of rate equations).

APPENDIX: UNSTABLE HYSTERESIS LOOPS GENERATED BY A SQ WAVE

For the sake of simplicity, the calculation is limited to a system of collinear monodisperse nanoparticles with $\phi = 0$. It is assumed that when the magnetic field switches from positive to negative and viceversa the occupancy numbers n_{10} and n_{20} do not change (ideally adiabatic loop branches). As a consequence, in this approximation the hysteresis loop is a perfect rectangle with horizontal and vertical sides in the (h, m) plane; the ordinates of the adiabatic branches are equal to the upper and lower remanence.

With reference to the left panel of Figure 10, the first magnetization curve $(O \rightarrow F)$ lies on the horizontal axis. On the vertical segments the system relaxes towards the equilibrium magnetization $m_{eq} \equiv m_{eq}(h_v)$. The first relaxation process $(n = 1, \; F \rightarrow A)$ brings the

magnetization from zero to the value $m_{1f} = m_{eq}(1 - z)$ where

$$z = e^{-y/2f\tau^0_{rel}}.$$

Here $yT/2 \equiv y/2f$ is the time allowed to the system to relax at constant field and τ^0_{rel} is the relaxation time (see Equation 4) when $\phi = 0$. The second relaxation ($n = 2$; $B \rightarrow C$) brings the magnetization from $m_{2i} \equiv m_{1f}$ to $m_{2f} = -m_{eq}(1 - 2z + z^2)$. The third relaxation ($n = 3$; $D \rightarrow A'$) brings the magnetization from $m_{3i} \equiv m_{2f}$ to $m_{3f} = m_{eq}(1 - 2z + 2z^2 - z^3)$ and so on. Odd/even numbers indicate upward/downward relaxation paths. By induction it is easy to show that after a relaxation process labelled by the generic odd number $n = 2k - 1$ ($k = 1, 2, 3...$) one has:

$$m_{2k-1\,f}(k) = m_{eq} \ (1 - 2z + 2z^2 - ... + 2z^{2k-2} - z^{2k-1}) =$$
$$= m_{eq} \ \frac{1-z}{1+z} \ (1 + z^{2k-1}) \tag{A.1}$$

The last expression of Equation (A.1) is also the magnetic remanence on the upper branch of the loop, $m_{RUP}(k)$. After a relaxation process labelled by the generic even number $n = 2k$ ($k = 1, 2, 3...$) one has instead:

$$m_{2k\,f}(k) = -m_{eq} \ (1 - 2z + 2z^2 - ... - 2z^{2k-1} + z^{2k}) =$$
$$= -m_{eq} \ \frac{1-z}{1+z} \ (1 - z^{2k}) \tag{A.2}$$

the last expression in Equation (A.2) being the lower-branch remanence $m_{RLO}(k)$. The arithmetic sum $S(k)$ of the two remanence values is:

$$S(k) = m_{eq}z^{2k-1}(1 - z)$$

Generally speaking, upper and lower remanence are different in absolute value. In particular, when $k = 1$ one has:

$$m_{RUP}(1) = m_{eq}(1 - z)$$

$$m_{RLO}(1) = -m_{eq}(1 - z)^2$$

while for $k \to \infty$ the two remanences become equal in absolute value, and $S \to 0$:

$$lim_{k \to \infty} m_{RUP}(k) = m_{eq} \frac{1 - z}{1 + z}$$

$$lim_{k \to \infty} m_{RLO}(k) = -m_{eq} \frac{1 - z}{1 + z}$$

$$lim_{k \to \infty} S(k) = 0$$

When $z \to 0$, i.e., when the time $yT/2 = y/2f$ allowed to the system to relax at constant field is much longer than the relaxation time τ_{rel}^0, the two remanences are equal since the first loop (no loop instability). On the contrary, when z is appreciably greater than zero an initial instability of the loop appears: the trajectories of instable loops do not close on themselves (the first complete loop having vertexes A, B, C, D, A', the second one A', B', C', D', A'' and so on (see left panel of Figure 10)); the steady state corresponding to closed magnetization loops is reached after a sequence of iterations.

In the former case, the system has enough time to reach the equilibrium magnetization at the field h_v; else, relaxation stops with the system being still away from the equilibrium value. Therefore, the more far away from equilibrium is vertex A, the more instable the loop. This can be checked in the upper right panel of Figure 10 where two instable loops are shown, the one drawn with red lines having the vertex A much closer to the corresponding equilibrium magnetization (dashed line). In the lower panel, the different evolution of $m_{RUP}(k)$ and $m_{RLO}(k)$ with k is shown for both cases. The full symbols are the values predicted by Equations (A.1) and (A.2); the open symbols are the remanences taken on the loops calculated solving the full rate equations. The perfect agreement between the two

datasets means that the starting approximations are suitable to describe the effect.

REFERENCES

[1] D. Ortega, and Q. A. Pankhurst, Magnetic hyperthermia in *Nanoscience: Volume 1: Nanostructures through Chemistry* edited by P. O'Brien (Royal Society of Chemistry: Cambridge, 2013) Chapter 3, pp. 60-88.

[2] Suriyanto, E. Y. K. Ng, and S. D. Kumar, Physical mechanism and modeling of heat generation and transfer in magnetic fluid hyperthermia through NÃľelian and Brownian relaxation: a review, BioMed. Eng. OnLine **16**, (2017).

[3] Z. Shaterabadi, G. Nabiyouni, and M. Soleymani, Physics responsible for heating efficiency and self-controlled temperature rise of magnetic nanoparticles in magnetic hyperthermia therapy, Prog. Biophys. Mol. Biol. **133**, 9, (2018).

[4] K. Mahmoudi, A. Bouras, D. Bozec, R. Ivkov, and C. Hadjipanayis, Magnetic hyperthermia therapy for the treatment of glioblastoma: a review of the therapyâĂŹs history, efficacy, and application in humans, Int. J. Hyperther. **34**,1316, (2018).

[5] M-K. Kim, J. Sim, J-H. Lee, M. Kim, and S-K. Kim, Dynamical Origin of Highly Efficient Energy Dissipation in Soft Magnetic Nanoparticles for Magnetic Hyperthermia Applications, Phys. Rev. Appl. **9**,054037, (2018).

[6] D. Chang, M. Lim, J. A. C. M. Goos, R. Qiao, Y. Y. Ng, F. M. Mansfeld, M. Jackson, T. P. Davis, and M. Kavallaris, Biologically Targeted Magnetic Hyperthermia: Potential and Limitations, Front. Pharmacol. **9**, 813, (2018).

[7] P. Das, M. Colombo, and D. Prosperi, Recent advances in magnetic fluid hyperthermia for cancer therapy, Colloids Surf. B Biointerfaces **174**, 42, (2019).

[8] G. Cai, S. Park, X. Cheng, A. L-S. Eh, and P. S. Lee, Inkjet-printed metal oxide nanoparticles on elastomer for strain-adaptive transmissive electrochromic energy storage systems, Sci. Technol. Adv. Mat. **19**, 759, (2018).

[9] Y. Bao, J. A. Sherwood, and Z. Sun, Magnetic iron oxide nanoparticles as T_1 contrast agents for magnetic resonance imaging, J. Mater. Chem. C **6**, 1280, (2018).

[10] W. Zhang, L. Liu, H. Chen, K. Hu, I. Delahunty, S. Gao, and J. Xie, Surface impact on

nanoparticle-based magnetic resonance imaging contrast agents, Theranostics **8**, 2521, (2018).

[11] K. El-Boubbou, Magnetic iron oxide nanoparticles as drug carriers: preparation, conjugation and delivery, Nanomedicine (Lond) **13**, 929, (2018).

[12] T. Vangijzegem, D. Stanicki, and S. Laurent, Magnetic iron oxide nanoparticles for drug delivery: applications and characteristics, Expert Opin. Drug Del. **16**, 69, (2019).

[13] N. LÃűwa, J-M. Fabert, D. Gutkelch, H. Paysen, O. Kosch, F. Wiekhorst, 3D-printing of novel magnetic composites based on magnetic nanoparticles and photopolymers, J. Magn. Magn. Mater. **469**, 456 (2019).

[14] H. Ceylan, I. C. Yasa, O. Yasa, A. F. Tabak, J. Giltinan, and M. Sitti, 3D-Printed Biodegradable Microswimmer for Theranostic Cargo Delivery and Release, ACS Nano **13**, 3353, (2019).

[15] M. Basini, A. Guerrini, M. Cobianchi, F. Orsini, D. Bettega, M. Avolio, C. Innocenti, C. Sangregorio, A. Lascialfari, and P. Arosio, Tailoring the magnetic core of organic-coated iron oxides nanoparticles to influence their contrast efficiency for Magnetic Resonance Imaging, J. Alloy. Compd. **770**, 58 (2019).

[16] J. Wolfram, and M. Ferrari, Clinical cancer nanomedicine, Nano Today **25**, 85 (2019).

[17] Y-L. Liu, D. Chen, P. Shang, and D-C. Yin, A review of magnet systems for targeted drug delivery, J. Control. Release **302**, 90 (2019)

[18] B. Kozissnik, A. C. Bohorquez, J. Dobson, and C. Rinaldi, Magnetic fluid hyperthermia: Advances, challenges, and opportunity, Int. J. Hyperther. **29**, 706, (2013).

[19] G. Bellizzi, and O. M. Bucci, Magnetic Nanoparticle Hyperthermia in *Emerging Electromagnetic Technologies for Brain Diseases Diagnostics, Monitoring and Therapy* edited by L. Crocco, I. Karanasiou, M. L. James, R. Cruz Conceição (Springer, Cham, 2018) Chapter 6, pp. 129-191.

[20] V. Fernandes Cardoso, A. Francesko, C. Ribeiro, M. Bañobre-López, P. Martins, and S. Lanceros-Mendez, Advances in Magnetic Nanoparticles for Biomedical Applications, Adv. Healthcare Mater **7**, 1700845 (2018).

[21] L. Beola, L. GutiérrezâĂă, V. Grazú, and L. Asín A Roadmap to the Standardization of In Vivo Magnetic Hyperthermia in *Nanomaterials for Magnetic and Optical Hyperthermia Applications* edited by R. M. Fratila and J. M. De La Fuente (Elsevier, 2019) and references therein.

[22] G. Bell, L. K. Bogart, P. Southern, M. Olivo, Q. A. Pankhurst, and I. P. Parkin, Enhancing the Magnetic Heating Capacity of Iron Oxide Nanoparticles through Their Postproduction Incorporation into Iron OxideâĂŞGold Nanocomposites, Eur. J. Inorg. Chem. **2017**, 2386 (2017).

[23] J. Mohapatra, F. Zeng, K. Elkins, M. Xing, M. Ghimire, S. Yoon, S. R. Mishra and J. Ping Liu, Size-dependent magnetic and inductive heating properties of Fe_3O_4 nanoparticles: scaling laws across the superparamagnetic size, Phys.Chem.Chem.Phys. **20**, 12879 (2018).

[24] B. B. Lahiri, S. Ranoo, J. Philip, Effect of orientational ordering of magnetic nanoemulsions immobilized in agar gel on magnetic hyperthermia J. Magn. Magn. Mater. **451**, 254 (2018).

[25] G. Kandasamy, A. Sudame, P. Bhati, A. Chakrabarty, and D. Maity, Systematic investigations on heating effects of carboxyl-amine functionalized superparamagnetic iron oxide nanoparticles (SPIONs) based ferrofluids for in vitro cancer hyperthermia therapy, J. Mol. Liq. **256**, 224 (2018).

[26] G. Shi,R. Takeda,S. B. Trisnanto, T. Yamada, S. Ota, and Y. Takemura, Enhanced specific loss power from ResovistÂő achieved by aligning magnetic easy axes of nanoparticles for hyperthermia, J. Magn. Magn. Mater. **473**, 148 (2019).

[27] A. Nikitin, M. Khramtsov, A. Garanina, P. Mogilnikov, N. Sviridenkova, I. Shchetinin, A. Savchenko, M. Abakumov, and A. Majouga, Synthesis of iron oxide nanorods for enhanced magnetic hyperthermia, J. Magn. Magn. Mater. **469**, 443 (2019).

[28] R. Hergt, S. Dutz and M. Zeisberger, Validity limits of the Néel relaxation model of magnetic nanoparticles for hyperthermia, Nanotechnology **21**, 015706 (2010).

[29] S. Dutz and R. Hergt, Magnetic particle hyperthermia - a promising tumour therapy?, Nanotechnology **25**, 452001 (2014)

[30] N. A. Usov, Low frequency hysteresis loops of superparamagnetic nanoparticles with uniaxial anisotropy, J. Appl. Phys. **107**, 123909, (2010).

[31] T. J. Fal, M. L. Plumer, J. P. Whitehead, J. I. Mercer, J. van Ek, and K. Srinivasan, Simulations of magnetic hysteresis loops for dual layer recording media, Appl. Phys. Lett. **102**, 202404, (2013).

[32] L. Néel, Théorie du trainage magnétique des ferromagnétiques en grains fins avec applications aux terres cuites, Ann. Geophys. (C.N.R.S.), **5**, 99 (1949).

[33] P. Allia, G. Barrera and P. Tiberto, Linearized rate-equation approach for double-well systems: Cooling- and temperature-dependent low-field magnetization of magnetic nanoparticles, Phys. Rev. B **98**, 134423 (2018).

[34] A. P. Guimaraes, *Principles of Magnetism* (Springer, 2009).

[35] N. A. Usov, and Yu. B. Grebenshchikov, Superparamagnetic relaxation time of a single-domain

particle with a nonaxially symmetric double-well potential, J. Appl. Phys. **105**, 043904 (2009).

[36] W. F. Brown Jr., Thermal Fluctuations of a Single-Domain Particle, Phys. Rev. **130**, 1677, (1963).

[37] Y. P. Kalmykov, The relaxation time of the magnetization of uniaxial single-domain ferromagnetic particles in the presence of a uniform magnetic field, J. Appl. Phys. **96**, 1138, (2014).

[38] N. A. Usov, and Yu. B. Grebenshchikov, Hysteresis loops of an assembly of superparamagnetic nanoparticles with uniaxial anisotropy, J. Appl. Phys. **106**, 023917, (2009).

[39] M. Morgan, and R. H. Victora, Use of square waves incident on magnetic nanoparticles to induce magnetic hyperthermia for therapeutic cancer treatment, Appl. Phys. Lett. **97**, 093705, (2010).

[40] M. Morgan, H. Sohn, and R. H. Victora, Use of trapezoidal waves and complementary static fields incident on magnetic nanoparticles to induce magnetic hyperthermia for therapeutic cancer treatment, J. Appl. Phys. **109**, 07B305, (2011).

[41] M. Knobel, W. C. Nunes, L. M. Socolovsky, E. De Biasi, J. M. Vargas, and J. C. Denardin, Superparamagnetism and Other Magnetic Features in Granular Materials: A Review on Ideal and Real Systems, J. Nanosci. Nanotechnol. **8**, 2836 (2008).

[42] M. Jeun, S. Bae, A. Tomitaka, Y. Takemura, K. H. Park, S. H. Paek and K. Chung, Effects of particle dipole interaction on the ac magnetically induced heating characteristics of ferrite nanoparticles for hyperthermia, Appl. Phys. Lett. **95**, 082501 (2009)

[43] C. Haase and U. Nowak, Role of dipole-dipole interactions for hyperthermia heating of magnetic nanoparticle ensembles, Phys. Rev. B **85**, 045435 (2012)

[44] B. Mehdaoui, R. P. Tan, A. Meffre, J. Carrey, S. Lachaize, B. Chaudret and M. Respaud, Phys. Rev. B **87**, 174419 (2013)

[45] L. C. Branquinho, M. S. Carriao, A. S. Costa1, N. Zufelato, M. H. Sousa, R. Miotto, R. Ivkov and A. F. Bakuzis, Sci. Rep. **3**, 2887 (2013)

[46] S. Ruta, R. Chantrell and O. Hovorka, Unified model of hyperthermia via hysteresis heating in systems of interacting magnetic nanoparticles, Sci. Rep. **5**, 9090 (2015)

[47] I. Conde-Leborán, D. Serantes, and D. Baldomir, Orientation of the magnetization easy axes of interacting nanoparticles: Influence on the hyperthermia properties, J. Magn. Magn. Mater. **380**, 321, (2015)

[48] N. A. Usov, O. N. Serebryakova and V. P. Tarasov, Interaction Effects in Assembly of Magnetic Nanoparticles, Nanoscale Res. Lett. **12**, 489 (2017)

[49] H. El Mrabti, P. M. Déjardin, S. V. Titov and Y. P. Kalmykov, Damping dependence in dynamic magnetic hysteresis of single-domain ferromagnetic particles, Phys. Rev. B **85**, 098425 (2012).

[50] S. Albert, M. Michl, P. Lunkenheimer, A. Loidl, P. M. Déjardin and F. Ladieu, Third and fifth harmonic responses in viscous liquids, Appendix 3, in *Nonlinear Dielectric Spectroscopy* edited by R. Richert (Springer, 2018) and references therein

[51] J. Carrey, B. Mehdaoui and M. Respaud, Simple models for dynamic hysteresis loop calculations of magnetic single-domain nanoparticles: Application to magnetic hyperthermia optimization, J. Appl. Phys. **109**, 083921 (2011)

[52] W. J. Atkinson, I. A. Brezovich and D. P. Chakraborty, IEEE Trans. Biomed. Engin. **31**, 70 (1984)

[53] S. Dutz and R. Hergt, Magnetic nanoparticle heating and heat transfer on a microscale:Basic principles, realities and physical limitations of hyperthermia for tumour therapy, Int J Hyperthermia **29**, 790 (2013)

[54] D. Bobo, K. J. Robinson, J. Islam, K. J. Thurecht and S. R. Corrie1, Nanoparticle-Based Medicines: A Review of FDA-Approved Materials and Clinical Trials to Date, Pharm. Res. **33**, 2373 (2016)

[55] R. Di Corato, A. Espinosa, L. Lartigue, M. Tharaud, S. Chat, T. Pellegrino, C. Ménager, F. Gazeau and C. Wilhelm, Magnetic hyperthermia efficiency in the cellular environment for different nanoparticle designs, Biomater. **35**, 6400 (2014)

[56] D. Soukup, S. Moise, E. Céspedes, J. Dobson and N. D. Telling, In-Situ Measurement of Magnetisation Relaxation of Internalised Nanoparticles in Live Cells, ACSNano **9**, 231 (2015)

[57] B. D. Cullity and C. D. Graham, *Introduction to Magnetic Materials* (IEEE press, Wiley, 2009), Ed. 2.

[58] A. Jordan, R. Scholz, K. Maier-Hau, M. Johannsen, P. Wust, J. Nadobny, H. Schirra, H. Schmidt, S. Deger, S. Loening, W. Lanksch and R. Felix, Presentation of a new magnetic field therapy system for the treatment of human solid tumors with magnetic fluid hyperthermia, J. Magn. Magn. Mater. **225**, 118 (2001)

[59] R. E. Rosensweig, Heating magnetic fluid with alternating magnetic field, J. Magn. Magn. Mater. **252**, 370 (2002).

[60] see, e.g.,: *Health Council of the Netherlands: ELF Electromagnetic Fields Committee. Exposure to electromagnetic fields (0 Hz - 10 MHz). The Hague: Health Council of the Netherlands,*

publication no. 2000/06E, ISBN: 90-5549-311-2 (2000)

[61] Q. A. Pankhurst, N. T. K. Thanh, S. K. Jones and J. Dobson, J. Phys. D: Appl. Phys. **42**, 224001 (2009)